this study, is well capable to simulate tropospheric chemistry involving ozone with detailed schemes for chemical and physical processes. Future model development will be focused on improvement of the transport scheme in the model. Also, more detailed aqueous-phase chemistry will be included in future versions of CHASER.

Appendix 2A: Evaluation of transport and deposition processes

Evaluation: Transport process

Transport is one of the most important processes to simulate the atmospheric photochemistry. Emitted or chemically produced species undergo advection by large-scale wind field and subgrid vertical transport by diffusion and moist convection. In CHASER, advective transport is simulated by a 4th order flux-form advection scheme of the monotonic van Leer [*van Leer*, 1977], except for the vicinity of the poles (the flux-form semi-Lagrangian scheme of *Lin and Rood* [1996] is used for a simulation of advection around the poles), with vertical transport associated with moist convection (updrafts and downdrafts) simulated by the cumulus convection scheme in the CCSR/NIES AGCM.

It is necessary to validate the model capability for simulations of transport. For this purpose, we have conducted a simple simulation of the distribution of atmospheric radon (^{222}Rn). Radon is emitted from the earth's surface (mainly from land surface) and decays radioactively with a lifetime of 5.5 days. Surface emission of radon considered here is generally based on *Jacob et al.* [1997]. In *Jacob et al.* [1997], radon emission from land surface is set 1.0 atoms cm^{-2} s^{-1} uniformally. Some simulation studies based on this radon emission scenario, however, show an underestimation of the simulated radon concentrations at Mauna Loa by a factor of 2-3 compared to observations, with showing relatively good agreement of simulations with observations at other sites [*Jacob et al.*, 1997; *Brasseur et al.*, 1998]. Although there is a possibility that an insufficient transport in the simulations causes this discrepancy on one side, it can be attributed to a higher emission rate of radon in eastern Asia as suggested by *Mahowald et al.* [1997]. To take this into account, emission rate in eastern Asia (10°S-55°N, 100°E-160°E) is tentatively increased by a factor of 2 in this simulation.

Figure 2A.1 shows the simulated radon distributions for June-July-August (JJA). As can be seen in zonal mean distribution (upper panel), radon is vertically transported from the surface up to the tropopause height associated with convective activities in the northern hemisphere. Horizontal distribution of radon in the upper troposphere can be seen in the lower panel of Figure 2A.1. Outstanding high concentrations over eastern Asia are due to the doubled emission rate in this region. Transport of radon from northern America and Africa to over the Atlantic is seen. Moreover, long range transport of radon from eastern Asia appears to reach the eastern Pacific region including western America. Figure 2A.2 compares the simulated and the observed radon vertical profiles in western America (California) for June and JJA conditions. The model appears to reproduce the observed radon vertical distribution in the middle-upper troposphere well. The radon maximum

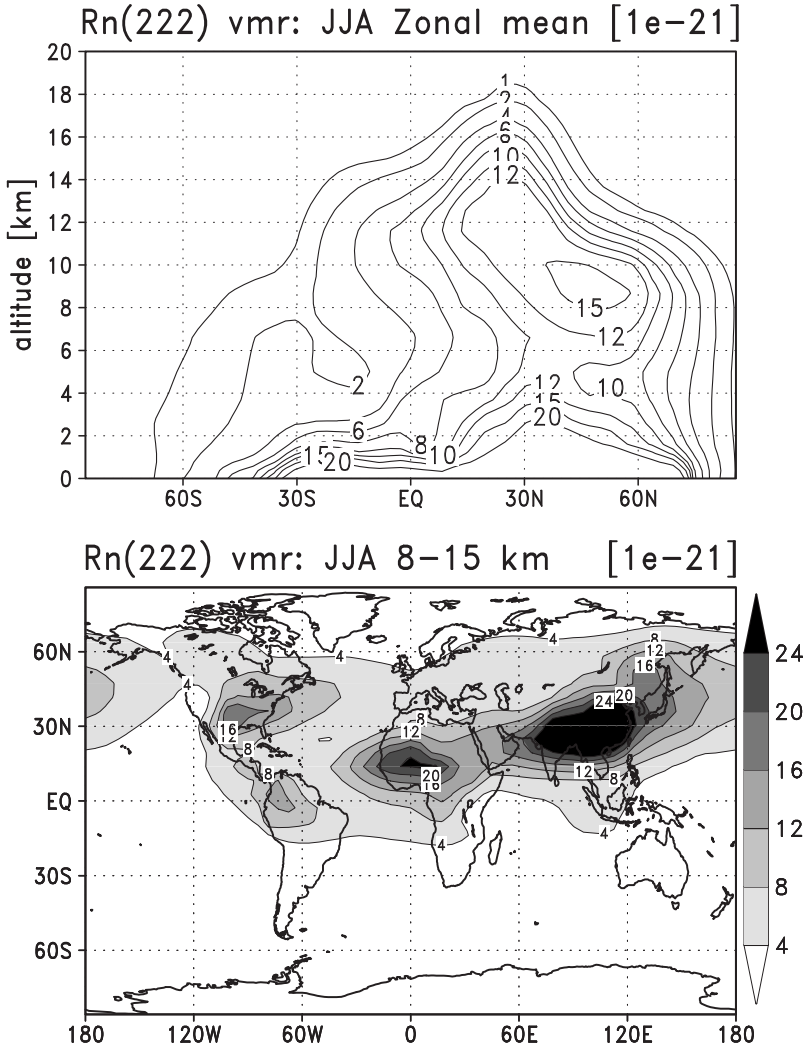

Figure 2A.1. Calculated distributions (volume mixing ratio) of radon for June-July-August. The distribution in the upper panel is zonally averaged, and averaged over 8-15 km altitude for the lower panel

seen at 8-10 km altitude is much associated with long range transport from eastern Asia, according to *Stockwell et al.* [1998]. This feature is clearly seen in Figure 2A.3 showing the cross sectional distribution of calculated radon over 36°N for June. It can be seen that the radon distribution in the middle-upper troposphere is largely affected by transport from eastern Asia through much of the eastern Pacific and western America. In Figure 2A.2, radon concentration is slightly underestimated by the model in 1-3 km altitudes, whereas it is overestimated at the surface. This may indicate an insufficient mixing between the planetary boundary layer and the lower troposphere. Figure 2A.4 shows a comparison of calculated and observed seasonal variations of surface radon at several sites. The model appears to reproduce observed radon seasonal cycle well. Both the concentration and the time variability of calculated surface radon are generally high in winter time when vertical transport of emitted radon is not efficient due to low convective activity. The seasonal

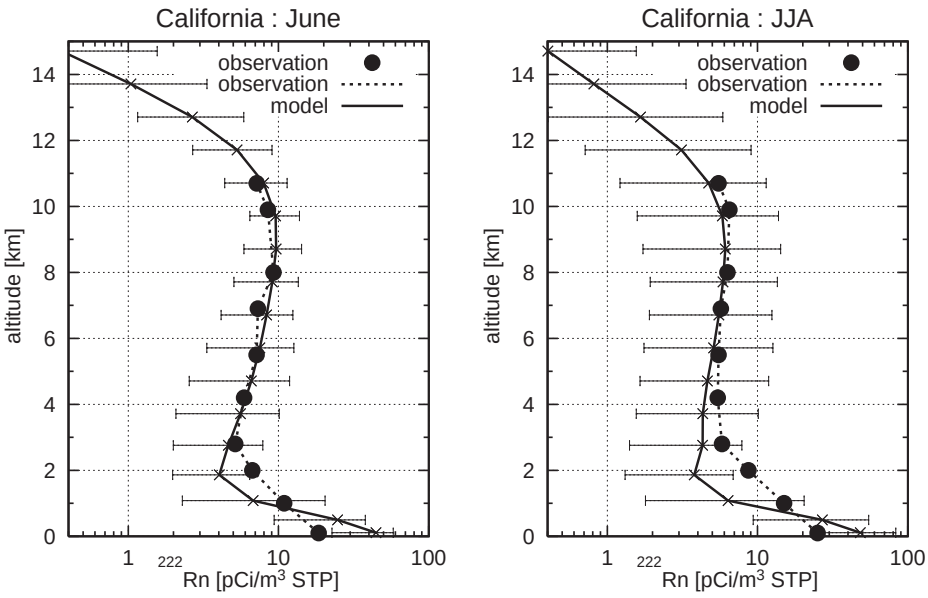

Figure 2A.2. Calculated (solid lines) and observed (solid circles and dashed lines) radon vertical profiles in California (37.4°N, 122°W). The values are June average (left panel) and June-July-August average (right panel). Error bars with calculated profiles show the range. Observation is from *Kritz et al.* [1998].

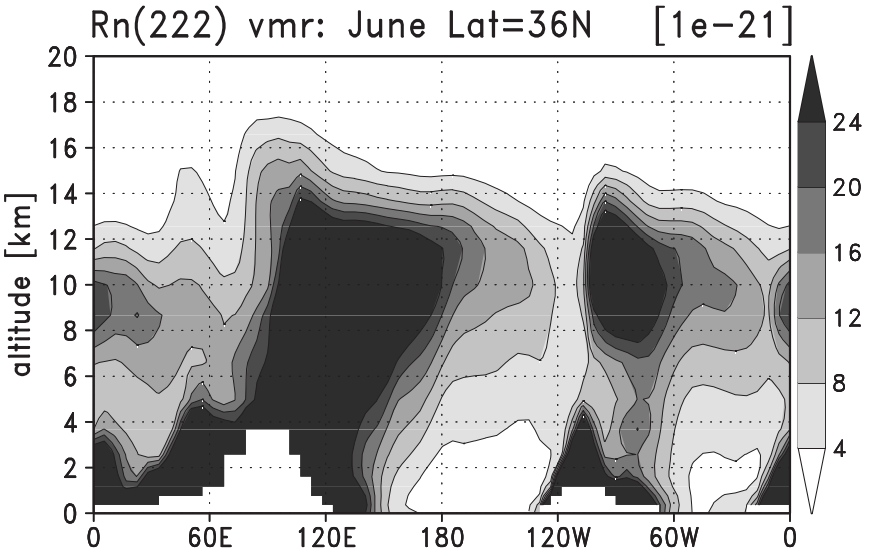

Figure 2A.3. Calculated distribution (volume mixing ratio) of radon in June for 36°N.

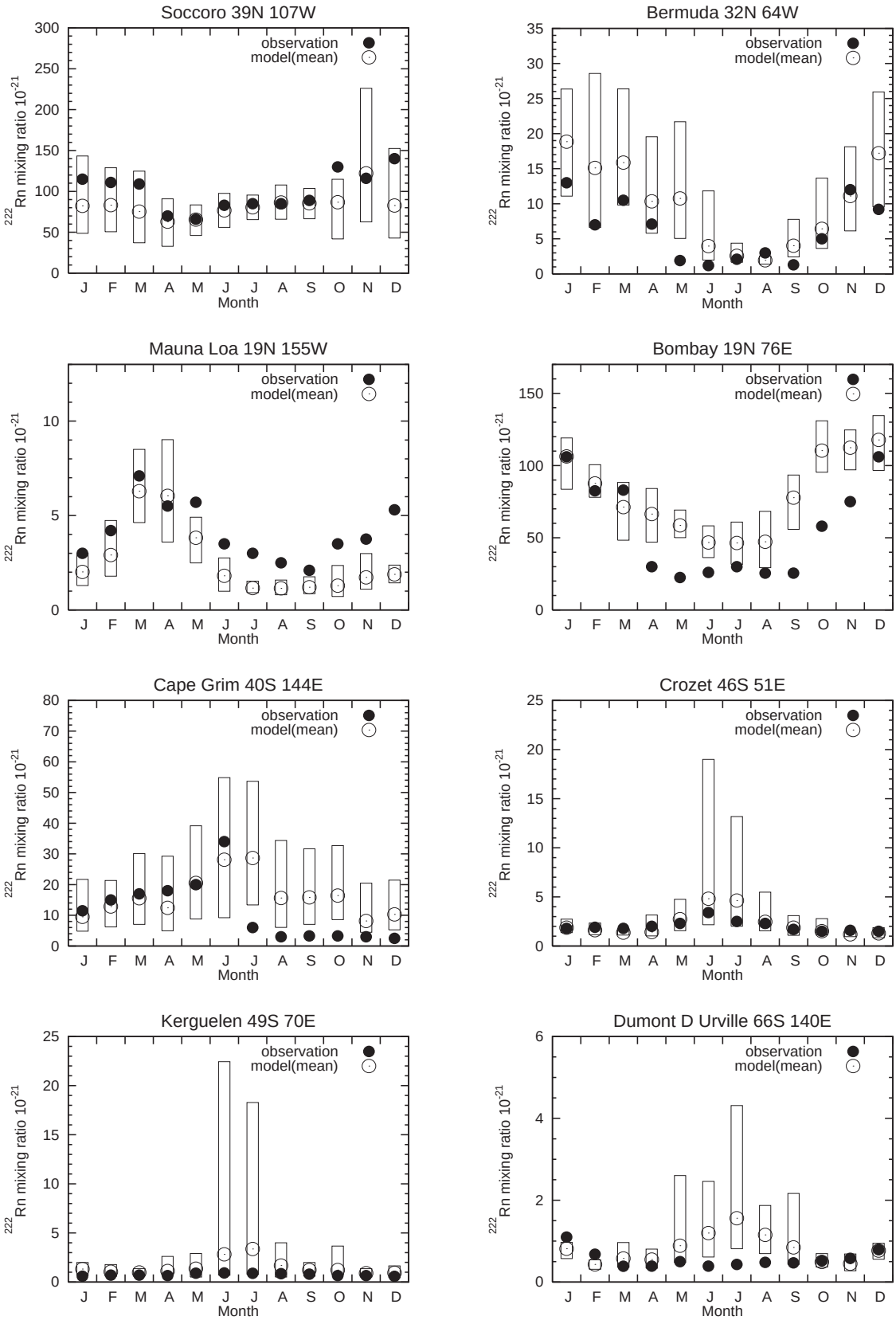

Figure 2A.4. Calculated (open circles) and observed (solid circles) surface radon (^{222}Rn) seasonal variations. Boxes show the range of calculated values.

cycle of spring-maximum at Mauna Loa is also well reproduced with the doubled radon emission in eastern Asia.

Evaluation: Deposition process

For an evaluation of the wet deposition scheme as described in section 2.2.3, we have conducted a simulation using atmospheric lead (^{210}Pb) as a tracer. This simulation has been performed as an extension of the simulation of ^{222}Rn described right above, since ^{210}Pb is produced by radioactive decay of ^{222}Rn. ^{210}Pb produced from ^{222}Rn, believed to stick to aerosol surfaces rapidly, was assumed to efficiently removed by wet deposition with the same scavenging lifetime for HNO_3 as in many other simulations [*Balkanski et al.*, 1993; *Lee and Feichter*, 1995; *Rehfeld and Heimann*, 1995; *Brasseur et al.*, 1998]. Note that the reemission process below clouds as described in section 2.2.3 is not considered in this ^{210}Pb simulation. The dry deposition velocity of ^{210}Pb at the surface is taken to be 0.2 cm s^{-1} over land surface and 0.05 cm s^{-1} over sea surface, following *Balkanski et al.* [1993].

Figure 2A.5 shows a comparison of the mixing ratios of ^{210}Pb calculated and observed at the surface. The seasonal variations of ^{210}Pb are well reproduced by the model for all sites. For Mauna Loa, calculated values are in good agreement with the observation because of our augmentation of radon emission in eastern Asia (see above). Although Figure 2A.5 indicates that the model successfully simulates the wet deposition process, it should be noted that there may be uncertainties in the surface emission of radon adopted here and precipitation simulated by the AGCM.

Appendix 2B: Aqueous-phase reactions in the model

In this study, the model includes liquid-phase oxidation of SO_2 in cloud drops, considering the tendency for S(IV), the sum of $SO_2(aq)$, HSO_3^-, and SO_3^{2-} in liquid-phase (Table 2B.1). The hydrogen ion concentration $[H^+]$ in cloud drops, needed for the A1 and A2 reactions, is given as:

$$[H^+] = f_n \times ([NO_3^-] + [SO_4^{2-}] + [HSO_3^-] + [SO_3^{2-}]) \tag{2B.1}$$

using the neutralizing factor f_n to consider neutralization by cations, and the liquid-phase concentrations (eq l^{-1}) of NO_3^-, SO_4^{2-}, HSO_3^-, and SO_3^{2-}. In this study, f_n has been taken to be 0.1-0.2 to simulate $[H^+]$ close to observations. The gas/liquid partitioning for "SO_2(g) $\leftrightarrow$ S(IV)", "O_3(g) $\leftrightarrow$ O_3(aq)", and "H_2O_2(g) $\leftrightarrow$ H_2O_2(aq)" is determined from the effective Henry's law constants H for SO_2, O_3, and H_2O_2. In the case of SO_2(g) $\leftrightarrow$ S(IV), H is calculated depending on $[H^+]$ as:

$$H(SO_2) = 1.2 \exp\left[3200\left(\frac{1}{T} - \frac{1}{298.15}\right)\right] \cdot \left(1 + \frac{K_1}{[H^+]} + \frac{K_1 K_2}{[H^+]^2}\right) \tag{2B.2}$$

with the K_1 and K_2 the equilibrium constants for $SO_2(aq) \leftrightarrow HSO_3^-$ and $HSO_3^- \leftrightarrow SO_3^{2-}$ listed in Table 2B.1. This shows that dissolution of SO_2 in liquid-phase is highly limited by the $[H^+]$ level (i.e., pH), decreasing as pH in cloud drops becomes lower.

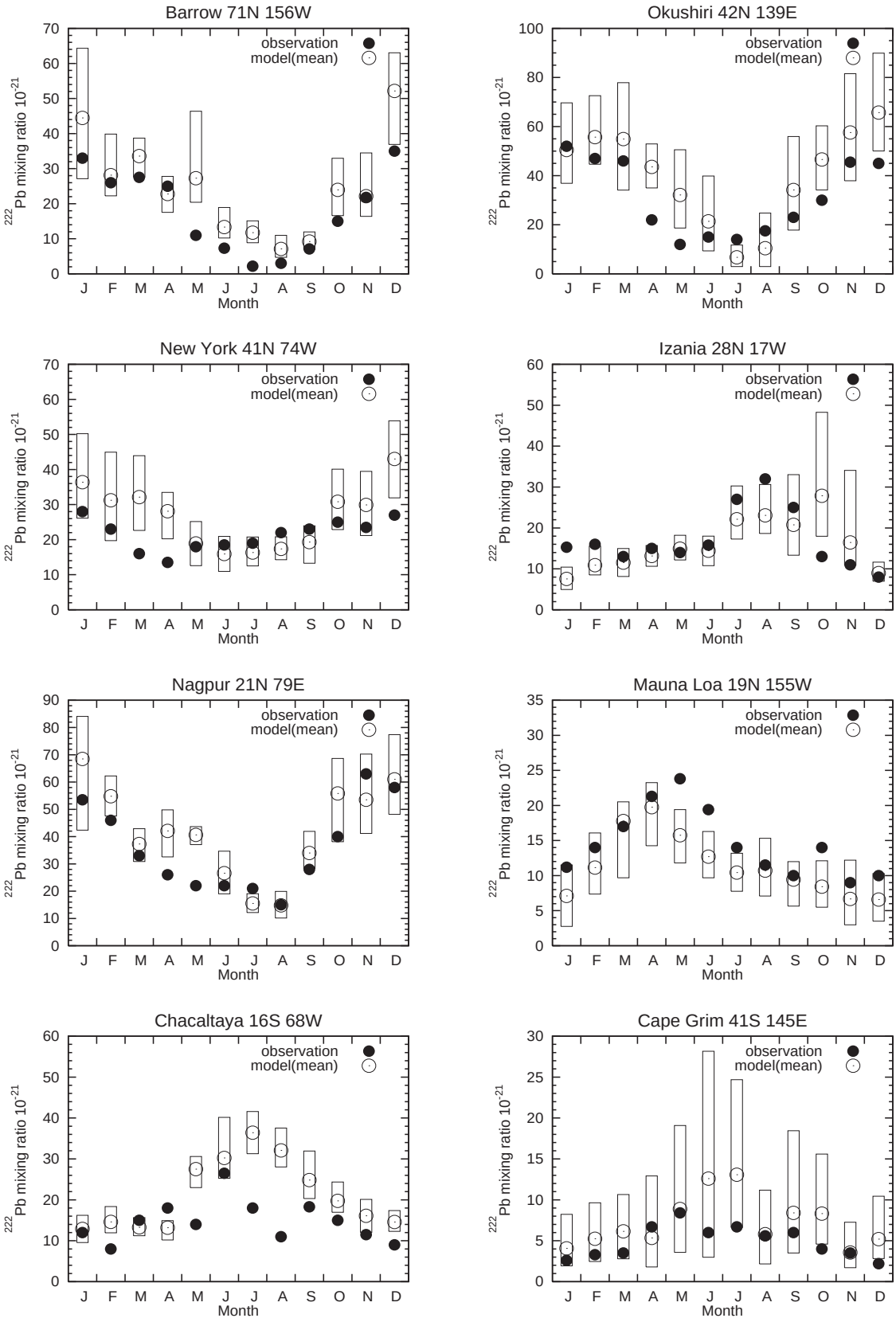

Figure 2A.5. Seasonal variations of calculated (solid circles) and observed (solid circles) surface lead (^{210}Pb). Boxes show the range of calculated values.

Table 2B.1. Aqueous-phase Oxidation of S(IV).

No.	Reaction	Rate[a]
A1	$S(IV) + O_3(aq) \rightarrow SO_4^{2-}$	$k_{A1} = \frac{k_1 + \frac{k_2 K_1}{[H^+]} + \frac{k_3 K_1 K_2}{[H^+]^2}}{1 + \frac{K_1}{[H^+]} + \frac{K_1 K_2}{[H^+]^2}}$, $k_1 = 2.4E+4$, $k_2 = 3.7E+5\ \exp(-5500(1/T-1/298.15))$, $k_3 = 1.5E+9\ \exp(-5300(1/T-1/298.15))$, K_1[b]$= 1.7E-2\ \exp(-2090(1/T-1/298.15))$, K_2[c]$= 6.0E-8\ \exp(-1120(1/T-1/298.15))$
A2	$S(IV) + H_2O_2(aq) \rightarrow SO_4^{2-}$	$k_{A2} = \frac{k_4[H^+]}{(0.1+[H^+])\left(1 + \frac{[H^+]}{K_1} + \frac{K_2}{[H^+]}\right)}$, $k_4 = 5.2E+6\ \exp\ (-2750(1/T-1/298.15))$

References: *Hoffmann and Calvert* [1985].
[a]K_{A1} and K_{A2} are in $l\ mol^{-1}\ s^{-1}$.
[b]Equilibrium constant for $SO_2(aq) \leftrightarrow HSO_3^-$
[c]Equilibrium constant for $HSO_3^- \leftrightarrow SO_3^{2-}$

To consider time integration of aqueous-phase reactions as listed in Table 2B.1, the model evaluates tendencies of bulk-phase (gas+liquid) concentrations in clouds. The tendency of a bulk-phase concentration C_i due to aqueous-phase reactions is given by:

$$\frac{dC_i}{dt} = P_i - \beta_i C_i = P_i^l L - \beta_i^l \frac{H_i RT \cdot L}{1 + H_i RT \cdot L} C_i \tag{2B.3}$$

with L the liquid water content, P^l the production rate in aqueous-phase (per unit volume of water), and β^l the loss rate for aqueous-phase concentrations due to aqueous-phase reactions. This tendency applies for SO_2, O_3, H_2O_2, and SO_4^{2-} with respect to the A1 and A2 reactions in this study. The tendency equations for those species are iteratively solved employing an implicit scheme (EBI scheme) with a time step of 10 min as with gas-phase reactions in the model.